Adjoint-Based Design of Rotors Using the Navier-Stokes Equations in a Noninertial Reference Frame

Eric J. Nielsen,[1] Elizabeth M. Lee-Rausch,[2] and William T. Jones[3]
NASA Langley Research Center, Hampton, Virginia 23681

Optimization of rotorcraft flowfields using an adjoint method generally requires a time-dependent implementation of the equations. The current study examines an intermediate approach in which a subset of rotor flowfields are cast as steady problems in a noninertial reference frame. This technique permits the use of an existing steady-state adjoint formulation with minor modifications to perform sensitivity analyses. The formulation is valid for isolated rigid rotors in hover or where the freestream velocity is aligned with the axis of rotation. Discrete consistency of the implementation is demonstrated by using comparisons with a complex-variable technique, and a number of single- and multi-point optimizations for the rotorcraft figure of merit function are shown for varying blade collective angles. Design trends are shown to remain consistent as the grid is refined.

---

[1] Research Scientist, Computational AeroSciences Branch, MS 128, Senior Member AIAA.
[2] Research Engineer, Computational AeroSciences Branch, MS 128, Senior Member AIAA.
[3] Computer Engineer, Advanced Engineering Environments Branch, MS 125, Member AIAA.

Nomenclature

C	Aerodynamic coefficient
C_Q	Rotor torque coefficient
C_T	Rotor thrust coefficient
$\mathbf{D}$	Vector of design variables
E	Total energy per unit volume, modulus of elasticity
$\bar{\mathbf{F}}_i, \bar{\mathbf{F}}_v$	Inviscid and viscous flux tensors
FM	Rotorcraft figure of merit function
$\bar{\mathbf{I}}$	Identity tensor
$\mathbf{K}$	Elasticity coefficient matrix
L	Lagrangian function
N	Number of composite objective functions
$\mathbf{Q}$	Vector of conserved variables
$\mathbf{R}$	Spatial residual vector
$\mathbf{S}$	Source term vector
S	Control volume surface area
T	Temperature
V	Volume of control volume
$\mathbf{X}$	Vector of grid coordinates
f	Objective function
g	Real-valued function
h	Step size
i	$\sqrt{-1}$
i, j, k	Indices
k	Thermal conductivity
m	Number of constraint function components
$\hat{\mathbf{n}}$	Outward-pointing normal vector
n	Number of objective function components

p	Pressure, exponent
$\mathbf{r}$	Position vector
t	Time
u_i	Cartesian directional displacements
u, v, w	Cartesian components of velocity
x	Independent variable
x_i	Cartesian coordinate directions
$\mathbf{\Lambda}_f$	Flowfield adjoint variable
$\mathbf{\Lambda}_g$	Grid adjoint variable
Θ	Blade collective setting
$\mathbf{\Omega}$	Angular velocity vector
α, ω	Weights
$\overline{\boldsymbol{\varepsilon}}$	Strain tensor
η	Spanwise station
λ, μ	Lamé constants
ρ	Density, KS multiplier
$\overline{\boldsymbol{\tau}}$	Viscous stress tensor
υ	Poisson's ratio
mp	Denotes multi-point quantity
$surf$	Denotes surface quantity
*	Denotes target quantity, optimal quantity

Introduction

Application of high-fidelity computational fluid dynamics (CFD) has become commonplace in the fixed-wing aerospace community. Software packages that solve the Euler and Reynolds-averaged Navier-Stokes equations on both structured and unstructured grids are now used routinely in the analysis and design of new configurations. Moreover, as algorithms and computer hardware have continued to mature, the use of formal design optimization techniques coupled with CFD methods has become viable for large-scale problems in aerospace design.

The application of high-fidelity CFD tools to the analysis and design of full rotorcraft configurations is considerably more challenging. Such flowfields are inherently unsteady, frequently involve fluid velocities that range from quiescent to transonic flow, and typically require the simulation of complex aerodynamic and aerostructural interactions between dynamic vehicle components. Recent literature suggests that the use of high-fidelity CFD methods in this regime is growing, but the computational cost that is required to capture the necessary spatial and temporal scales of a typical rotorcraft flowfield remains considerable.[1]-[9]

In the field of gradient-based design, adjoint methods are known to provide an extremely efficient means for computing sensitivity information. The cost of such methods is equivalent to the expense that is associated with solving the analysis problem and is independent of the number of design variables. Adjoint methods can also be used to perform mathematically rigorous mesh adaptation and error estimation. Significant success has been reported for the application of these techniques to steady problems; for example, see Refs. [10]-[13] and the efforts cited in Ref. [14].

In general, optimization and mesh adaptation for large-scale rotorcraft flows using adjoint methods require a time-dependent implementation of the equations. Considerable effort by a number of research groups is being focused in this area, and examples of the use of such approaches have recently emerged.[15]-[17] Despite the algorithmic efficiency, however, the computational cost of these general time-dependent approaches can be considerable, and the application of such methods to practical problems of engineering interest may remain prohibitively expensive for some time.

The goal of the current work is to develop, implement, and demonstrate an adjoint-based design capability for rotor configurations for which the analysis problem may be cast as a steady problem in a noninertial reference frame. This approach permits the use of an existing steady-state adjoint formulation with minor modifications to perform sensitivity analyses. The resulting formulation is valid for isolated rigid rotors in hover or where the freestream velocity is aligned with the axis of rotation.

Flow Equations

The governing equations for the flowfield are the compressible, perfect gas Reynolds-averaged Navier-Stokes equations written in a reference frame that is rotating with a constant angular velocity $\boldsymbol{\Omega}$:

$$\frac{\partial(\mathbf{Q}V)}{\partial t} + \oint_{\partial V} (\bar{\mathbf{F}}_i - \bar{\mathbf{F}}_v) \cdot \hat{\mathbf{n}} dS = \mathbf{S}, \tag{1}$$

where $\mathbf{Q}$ is the vector of volume-averaged conserved variables $\mathbf{Q} = [\rho, \rho u, \rho v, \rho w, E]^T$, $\hat{\mathbf{n}}$ is an outward-pointing unit normal, and V is the control volume bounded by the surface ∂V. The inviscid and viscous flux tensors are given by

$$\overline{\mathbf{F}}_i = \begin{bmatrix} \rho(\mathbf{u} - \boldsymbol{\Omega} \times \mathbf{r}) \\ \rho \mathbf{u}^T (\mathbf{u} - \boldsymbol{\Omega} \times \mathbf{r}) + p\overline{\mathbf{I}} \\ (\mathbf{u} - \boldsymbol{\Omega} \times \mathbf{r})(E + p) + (\boldsymbol{\Omega} \times \mathbf{r}) p \end{bmatrix} \tag{2}$$

and

$$\overline{\mathbf{F}}_v = \begin{bmatrix} 0 \\ \overline{\boldsymbol{\tau}} \\ \mathbf{u} \cdot \overline{\boldsymbol{\tau}} - k \nabla T \end{bmatrix}. \tag{3}$$

The source term $\mathbf{S}$ represents a Coriolis effect that results from the rotating frame of reference:

$$\mathbf{S} = \begin{bmatrix} 0 \\ -\rho(\boldsymbol{\Omega} \times \mathbf{u}) \\ 0 \end{bmatrix}. \tag{4}$$

Here, $\mathbf{u}$ is the absolute velocity vector $\mathbf{u} = [u, v, w]$, $\mathbf{r}$ is the position vector relative to the axis of rotation, and $\overline{\boldsymbol{\tau}}$ is the viscous stress tensor. The equations are closed with the perfect gas equation of state and an appropriate turbulence model for the eddy viscosity. For rotorcraft simulations, the formulation that is described here is applicable to rigid rotor geometries in either a hover or ascending/descending flight condition, where the freestream velocity vector is parallel to the angular velocity vector $\boldsymbol{\Omega}$.

References [18]-[21] describe the flow solver that is used in the current work. The code can be used to perform aerodynamic simulations across the speed range, and an extensive list of options and solution mechanisms is available for spatial and temporal discretizations on general static or dynamic mixed-element unstructured meshes that may or may not contain overset grid topologies.

In the current study, the spatial discretization uses a finite-volume approach in which the dependent variables are stored at the vertices of single-block tetrahedral meshes. Inviscid fluxes at cell interfaces are computed by using the upwind scheme of Roe,[22] and viscous fluxes are formed by using an approach that is equivalent to a central-difference Galerkin procedure. The eddy viscosity is modeled by using the one-equation approach of Spalart and Allmaras[23] with the source term modification proposed by Dacles-Mariani.[24] For the steady-state flows (relative to the noninertial reference frame) that are described in this study, temporal discretization is performed by using a

backward-Euler scheme with local time stepping. Scalable parallelization is achieved through domain decomposition and message-passing communication.

An approximate solution of the linear system of equations that is formed within each time step is obtained through several iterations of a multicolor Gauss-Seidel point-iterative scheme. The turbulence model is integrated all the way to the wall without the use of wall functions. The turbulence model is solved separately from the mean flow equations at each time step with a time integration and a linear system solution scheme that is identical to that employed for the mean flow equations.

Grid Equations

To deform the interior of the computational mesh as the surface grid evolves during a shape optimization procedure, the mesh is assumed to obey the linear elasticity equations of solid mechanics. These relations can be written as

$$\oint_{\partial V} \lambda \left(\sum_{i=1}^{3} \frac{\partial u_i}{\partial x_i} \right) \bar{\mathbf{I}} \cdot \hat{\mathbf{n}} dS + \oint_{\partial V} 2\mu \bar{\boldsymbol{\varepsilon}} \cdot \hat{\mathbf{n}} dS = 0 , \tag{5}$$

where

$$\bar{\boldsymbol{\varepsilon}} = \frac{1}{2} \left(\frac{\partial u_i}{\partial x_j} + \frac{\partial u_j}{\partial x_i} \right) \tag{6}$$

is the strain tensor, u_i is the displacement vector in each of the Cartesian coordinate directions x_i, and λ and μ are material properties of the elastic medium. The quantities λ and μ are related to Young's modulus E and Poisson's ratio υ through the following:

$$\lambda = \frac{\upsilon E}{(1+\upsilon)(1-2\upsilon)} \tag{7}$$

and

$$\mu = \frac{E}{2(1+\upsilon)} . \tag{8}$$

The system is closed with the specification of two of the four parameters λ, μ, E, and υ. In the current implementation, E is taken as inversely proportional to the distance from the nearest solid boundary, while Poisson's ratio is taken uniformly as zero. This approach forces cells that are near boundaries to move in a nearly rigid fashion, while cells that are far from the boundaries are allowed to deform more freely. The system of

equations is solved using GMRES[25] with either a point-implicit or ILU(0) preconditioning technique as described in Refs. [21] and [26].

Discrete Adjoint Equations

To derive the discrete adjoint equations, a compact notation is introduced for the governing equations that are outlined above. The spatial residual vector $\mathbf{R}$ of Eq. (1) is defined as

$$\mathbf{R} \equiv \oint_{\partial V} (\bar{\mathbf{F}}_i - \bar{\mathbf{F}}_v) \cdot \hat{\mathbf{n}} dS - \mathbf{S} . \tag{9}$$

Furthermore, the linear system of equations given by Eq. (5) can be written as

$$\mathbf{K}\mathbf{X} = \mathbf{X}_{surf} , \tag{10}$$

where $\mathbf{K}$ is the elasticity coefficient matrix that results from the discretization of Eq. (5), $\mathbf{X}$ is the vector of the grid-point coordinates, and $\mathbf{X}_{surf}$ is the vector of known surface grid-point coordinates, complemented by zeros for all interior coordinates.

With the approach that was taken in Ref. [11], a Lagrangian function can be defined as follows:

$$L(\mathbf{D},\mathbf{Q},\mathbf{X},\boldsymbol{\Lambda}_f,\boldsymbol{\Lambda}_g) = f(\mathbf{D},\mathbf{Q},\mathbf{X}) + \boldsymbol{\Lambda}_f^T \mathbf{R}(\mathbf{D},\mathbf{Q},\mathbf{X}) + \boldsymbol{\Lambda}_g^T (\mathbf{K}\mathbf{X} - \mathbf{X}_{surf}) , \tag{11}$$

where $\mathbf{D}$ represents a vector of design variables, f is an objective function, and $\boldsymbol{\Lambda}_f$ and $\boldsymbol{\Lambda}_g$ are the adjoint variables that multiply the residuals of the flow and the grid equations. In this manner, the governing equations may be viewed as constraints.

Differentiating Eq. (11) with respect to $\mathbf{D}$ and equating the $\partial\mathbf{Q}/\partial\mathbf{D}$ and $\partial\mathbf{X}/\partial\mathbf{D}$ coefficients to zero yields the discrete adjoint equations for the flowfield and grid, respectively:

$$\left[\frac{\partial \mathbf{R}}{\partial \mathbf{Q}}\right]^T \boldsymbol{\Lambda}_f = -\frac{\partial f}{\partial \mathbf{Q}} \tag{12}$$

and

$$\mathbf{K}^T \boldsymbol{\Lambda}_g = -\left\{\frac{\partial f}{\partial \mathbf{X}} + \left[\frac{\partial \mathbf{R}}{\partial \mathbf{X}}\right]^T \boldsymbol{\Lambda}_f\right\} . \tag{13}$$

The remainder of the terms in the linearized Lagrangian can be grouped to form an expression for the final sensitivity vector:

$$\frac{dL}{d\mathbf{D}} = \frac{\partial f}{\partial \mathbf{D}} + \boldsymbol{\Lambda}_f^T \frac{\partial \mathbf{R}}{\partial \mathbf{D}} - \boldsymbol{\Lambda}_g^T \left[\frac{\partial \mathbf{X}_{surf}}{\partial \mathbf{D}}\right] . \tag{14}$$

Eqs. (12) and (13) provide an efficient means for determining discretely consistent sensitivity information. The expense that is associated with solving these equations is independent of $\mathbf{D}$ and is similar to that of the governing equations. After the solutions for $\boldsymbol{\Lambda}_f$ and $\boldsymbol{\Lambda}_g$ have been determined, then the desired sensitivities may be calculated using Eq. (14), for which the computational cost is negligible.

A discrete adjoint implementation has been developed in Refs. [11], [17], [20], [26], and [27] for the flow solution method that is described above. The flowfield adjoint equations are solved in an exact dual manner, which ultimately guarantees an asymptotic convergence rate that is identical to the primal problem and costate variables that are discretely adjoint at every iteration of the solution process. The grid adjoint equations are solved by using GMRES in a manner that is identical to the method used for Eq. (5). To accommodate the noninertial reference frame that is used in the current study, minor modifications have been made to include the effects of the mesh speeds and the Coriolis terms.

Design Methodology

Design Variables

The implementation that is described in Ref. [11] is sufficiently general such that the user is able to employ a geometric parameterization scheme of choice, provided that the associated linearizations required by the adjoint method described above are also available. For the current study, the grid parameterization scheme that is described in Ref. [28] is used. This approach can be used to define very general shape parameterizations of existing grids by using a set of aircraft-centric design variables, such as camber, thickness, shear, twist, and planform parameters, at various locations on the geometry. The user also has the freedom to directly associate two or more design variables to create more general parameters. In the current work, this option is used to link several twist variables across the span of a rotor blade to create a single twist variable that is used to prescribe the blade collective setting Θ. In the event that multiple bodies of the same shape are to be designed – as in the case of rotor geometries – the implementation allows a single set of design variables to be used to simultaneously define such bodies. In this manner, the geometry of each body remains consistent throughout the course of the design.

Objective and Constraint Functions

The implementation that is described in Ref. [11] permits multiple objective functions f_i and explicit constraints c_j of the following form, each containing a summation of n_i and m_j individual components, respectively:

$$f_i = \sum_{k=1}^{n_i} \omega_k (C_k - C_k^*)^{p_k} \tag{15}$$

and

$$c_j = \sum_{k=1}^{m_j} \omega_k (C_k - C_k^*)^{p_k} \ . \tag{16}$$

Here, ω_k represents a user-defined weighting factor, C_k is an aerodynamic coefficient such as total drag or the pressure or viscous contributions to such quantities, and p_k is a user-defined exponent. The (*) superscript indicates a user-defined target value of C_k. Furthermore, the user may specify the boundaries in the grid to which each component function applies.

Design Points and Optimization Strategies

The current implementation supports an arbitrary number of user-specified design points at which objective and constraint functions may be posed. Each design point may be characterized by a variation of basic flowfield quantities such as the Mach number, or a more general characteristic such as the computational grid that is appropriate for each individual design point. In the current study, each blade collective setting Θ requires a different grid and, therefore, represents a different design point.

To perform multi-point optimization, three methods are considered. The first two approaches are unconstrained formulations for which individual objective functions f_i are posed at each design point, from which an overall composite objective function f_{mp} is constructed. The third approach is a constrained formulation.

The first method that is used to form the composite objective function f_{mp} defines a linear combination of f_i:

$$f_{mp} = \alpha_1 f_1 + \alpha_2 f_2 + \alpha_3 f_3 + \ldots + \alpha_N f_N \,, \tag{17}$$

where N is the total number of design points and α_i is a constant weighting factor that is applied to each individual f_i. In the current study, all values of α_i are chosen to be 1.0.

The second approach that is used to define f_{mp} is based on the technique described in Refs. [29] and [30]. In this approach, the objective functions f_i from each design point are combined by using the Kreisselmeier-Steinhauser function to form f_{mp} as

$$f_{mp} = f_{\max} + \frac{1}{\rho} \ln \left[\sum_{i=1}^{N} e^{\rho (f_i - f_{\max})} \right]. \tag{18}$$

The quantity $f_{\max}$ is defined as the maximum value over all f_i, and the value ρ is a user-defined constant that is taken to be 20.0.[30] Although not considered here, this approach also has the added benefit of being able to convert constrained optimization problems into unconstrained problems by including explicit constraints in the formulation of Eq. (18).

The third multi-point formulation that is considered is based on a constrained formulation. In this approach, the objective function to be minimized is defined at a single design point, while the objective functions that are defined at the other design points are instead treated as explicit constraints on the optimization problem.

The multi-point approaches that are used here are commonly used to obtain point solutions to multi-objective optimization problems via scalarization of the multiple objectives. The difficulty is that out of the range of many possible solutions only one is obtained by setting some parameters heuristically and externally, for example, the weights of the composite scalar objective. Because the current focus is the interaction of adjoint methods with design optimization, in principle the simple strategies that are adopted here suffice, but the related areas of robust and multi-objective design are extensive and active. The investigation of more sophisticated optimization strategies is relegated to future work.

For unconstrained problems, the optimization package that is described in Ref. [31] is used to minimize the specified objective function. In these cases, the optimizer is allowed to perform up to 20 design cycles or 30 function evaluations, whichever occurs first. The optimization algorithm considers the design converged and exits if it believes the following stopping tolerance is met:

$$\frac{f - f^*}{|f|} \leq 1 \times 10^{-5}, \tag{19}$$

where f^* is the objective function value at the optimal solution to the design problem and is not known a priori.

The package that is outlined in Ref. [32] is used for problems in which explicit constraints are present. The optimization algorithm is allowed to perform a maximum of 20 design cycles, and considers the design converged and exits if it believes the current objective function matches the value at the optimal solution to four significant digits. Constraints are considered satisfied if their values do not exceed the specified bounds by 0.5 percent of the bound value. The design at the initial choice of $\mathbf{D}$ is not required to satisfy the constraints; if needed, the optimizer attempts to locate a feasible starting point on its own.

Test Case

Demonstration optimizations are computed by using the three-bladed Tilt Rotor Aeroacoustics Model (TRAM) described in Refs. [33] and [34] and shown in Fig. 1. The optimizations are performed for a hover condition that corresponds to collective settings of $\Theta = 10^\circ$, $\Theta = 12^\circ$, and $\Theta = 14^\circ$. The tip Mach number is 0.62, and the Reynolds number is 2.1 million, based on the blade tip chord. The mesh that is used for the design studies contains 5,048,727 nodes and 29,802,252 tetrahedral elements and is designed for the $\Theta = 14^\circ$ setting. Grids for the $\Theta = 10^\circ$ and $\Theta = 12^\circ$ settings are obtained through elastic deformations of the baseline mesh. The surface grid for one of the blades is shown in Figure 2. All of the grids have been generated with the approach that is outlined in Ref. [35].

A geometric parameterization has been developed for the baseline blade geometry, as shown in Fig. 3. The approach yields a total of 44 active design variables, including 20 variables to control the blade thickness and 24 variables to control the blade camber. The root section of each blade is held fixed. Bounds on the design variables have been initially chosen with the intent to prevent nonphysical surface shapes; further constraints on the minimum thickness are described in a later section. The parameterization also allows for blade planform variations, as well as local twist and shearing deformations; however, these are held fixed in the current study.

For each design point, a single objective or constraint function is used, where $\omega = 1$, $p = 2$, and C is defined as the square of the commonly used rotorcraft figure of merit function, which is composed of the rotor thrust and torque coefficients:

$$C = FM^2 = \frac{C_T^3}{2C_Q^2}. \tag{20}$$

The square has been introduced to avoid the appearance of a square root of a negative thrust value in the linearized form of the objective function. In all cases, the value of C^* is chosen to be 2.0, which is considerably larger than both the baseline value at each of the collective settings examined here and the theoretical maximum value of 1.0.

All computations have been performed using 75 3.0-GHz dual-core Pentium IV processors with gigabit ethernet connections. A typical design cycle requires a single function and gradient evaluation for the current value of $\mathbf{D}$. A function evaluation in this context consists of an evaluation of the surface parameterization for each blade, a solution of Eq. (5) to deform the interior of the mesh according to the current surface grid, and a solution of the flow equations, Eq. (1). Using the adjoint approach that is outlined above, a gradient evaluation requires a solution of the flowfield adjoint equations, Eq. (12); a solution of the mesh adjoint equations, Eq. (13); an evaluation of the linearized surface parameterization for each blade; and finally, an evaluation of the gradient expression that is given

by Eq. (14). This combined procedure for obtaining a single function and gradient vector for a given collective setting Θ takes approximately 2.5 wall-clock hours with the use of the stated hardware. The convergence criteria that are used for each of the solvers has a direct impact on this efficiency. Finally, the time that is required to solve Eqs. (1) and (12) tends to decrease toward the end of an optimization as the design converges and the solution restarts become more effective.

Accuracy of Implementation

To verify that a discretely consistent implementation of Eqs. (12)-(14) has been achieved, the results are compared with those that are obtained with an independent approach based on the use of complex variables. This technique was originally suggested in Refs. [36] and [37], and was first applied to a Navier-Stokes solver in Ref. [38]. In this approach, a Taylor series with a complex step size ih is used to derive an expression for the first derivative of a real-valued function $g(x)$:

$$g'(x) = \frac{\mathrm{Im}\left[g\left(x + ih\right)\right]}{h} + O\left(h^2\right). \tag{21}$$

The primary advantage of this approach is that true second-order accuracy may be obtained by selecting step sizes without concern for the subtractive cancellation error that is typically present in real-valued divided differences. This capability can be immediately recovered at any time for the baseline solvers that are used in this study through the use of an automated scripting procedure as outlined in Ref. [39].

A coarse mesh that consists of 144,924 nodes and 848,068 tetrahedral elements is used to demonstrate the accuracy of the implementation for fully turbulent flow at the stated test conditions and a collective setting of $\Theta = 14^\circ$. Sensitivity derivatives of the figure of merit with respect to several shape parameters located at the midspan location of each blade are computed with the discrete adjoint implementation. The results are compared with values that were obtained with the complex variable method, where a step size of $h = 1 \times 10^{-30}$ was chosen. All equation sets are converged to machine precision by using 16 processors; the results are shown in Table 1. The sensitivity derivatives that are computed with the two methods are in excellent agreement.

Results

Single-Point Designs

The first set of results is a single-point design at each of the chosen blade collective settings. The history for the figure of merit during the course of each design is shown in Fig. 4. For each collective setting, the figure of merit

increases quickly during the early portion of the optimization, after which further gains are minimal. The initial and final figures of merit for each Θ are listed in Table 2. Improvements range from 4 percent to just under 8 percent, with smaller improvements at the higher collective settings. An expanded view of the resulting blade shape for each design is shown in Fig. 5, where the blades have each been rotated to the $\Theta = 14^\circ$ setting for comparison purposes. The design changes are similar at each collective setting: the camber has been increased across the majority of the span, while the thickness has been reduced. Of particular interest is the blade trailing edge, where each design has reduced the blade thickness to a numerically valid but physically infeasible dimension. Where the thickness is fixed at the blade tip, the optimization has increased the camber for the $\Theta = 10^\circ$ setting and decreased it for the other two collectives, most notably for the $\Theta = 14^\circ$ setting.

Single-Point Designs with Thickness Constraints

In an effort to achieve a more practical blade design in the trailing-edge region, the previous set of test cases was repeated. However, constraints were placed on the thickness variables to enforce the original blade thickness as a lower bound. The results with this approach are shown in Figs. 6 and 7. As before, the figure of merit for each collective setting increases rapidly during the initial portion of the optimization. Examination of the blade cross sections shows that the thickness of the baseline airfoil shape has been maintained as a lower bound. Differences between the designs at the various collective settings can be readily seen at the $\eta = 0.40$ station and at the blade tip. Table 3 shows the figure of merit results for each collective setting. The improvements are less than those observed for the cases in which blade thinning was allowed and range from almost 3 percent to 5.6 percent, with the largest improvements again taking place at the lower collective settings.

Multi-Point Designs

To evaluate the implementation for multi-point optimization problems, designs were performed by using the three strategies that were outlined earlier. For the approach that involved explicit constraints, the objective function was defined at the $\Theta = 14^\circ$ setting; the functions that were defined at the other two collective settings served as constraints. The lower bounds that were placed on these constraints correspond to the minimum figures of merit of 0.71 and 0.73 at the $\Theta = 10^\circ$ and $\Theta = 12^\circ$ settings, respectively. These choices represent moderate increases over the baseline figure of merit at each Θ based on the single-point design results. Note that because these constraints are not satisfied by the initial blade geometries in this approach, the optimization procedure must locate the feasible

region during the course of the design. The minimum thickness constraint is also enforced for each of the three multi-point approaches.

The convergence history for the approaches based on Eqs. (17) and (18) are shown in Figs. 8 and 9, respectively. The results for the two approaches are comparable for the figure of merit at each Θ. The final values, which are given in Tables 4 and 5, are also similar, although they are slightly higher for the approach based on the linear combination of individual objectives.

The convergence for the constrained approach is shown in Fig. 10. The blade design satisfies the constraints at $\Theta = 10^\circ$ and $\Theta = 12^\circ$ after the first design cycle, and the overall convergence for each collective setting is similar to the previous cases. However, note that for this particular case the optimization procedure was terminated early because of queue limitations on the computational platform. The procedure could be restarted if desired, but this was not pursued here. Table 6 shows that the final blade design with this approach yields figure of merit values that are comparable to those of the other multi-point approaches.

Although the final figures of merit that were obtained through each of the multi-point methods are similar, the differences in the optimized blade geometries are striking, as shown in Fig. 11. An investigation of the off-design performance for each blade geometry and the introduction of multidisciplinary interactions into the design process are logical next steps but are beyond the scope of the current work.

Effect of Grid Refinement

A grid-refinement study was performed by using the initial and final geometries that resulted from the multi-point optimizations described above. For these computations, a refined grid that consisted of 12,662,080 nodes and 87,491,279 tetrahedra was constructed and parameterized in a manner that was consistent with the baseline grid. The final design variables that were established in the multi-point optimizations were applied to the refined grid, and a single analysis was performed for each geometry to evaluate the resulting figure of merit. The results for the refined grid are included in parentheses in Tables 4-6 beneath the values for the baseline grid. Although the magnitude of the design improvements varies slightly with grid density, the results for the refined grid show similar trends in all cases as compared with the baseline mesh.

Concluding Remarks

A discrete adjoint-based methodology for performing design optimization of isolated rotor problems that appear as steady flows in a noninertial reference frame has been developed and implemented. The accuracy of the linearization has been established by comparing the results with an independent approach that is based on the use of

complex variables. A series of single- and multi-point designs at several blade collective settings showed improvements in the figure of merit function for both unconstrained and constrained problem formulations. Design trends were shown to remain consistent with grid refinement.

Ongoing efforts are focused on a general time-dependent adjoint-based optimization capability for rotorcraft, as well as for other aerospace configurations that are characterized by unsteady flowfields. The efficiency of such an implementation should be compared with that of the present approach, as well as with other techniques such as time-periodic formulations.

Acknowledgements

The authors wish to thank Dr. Natalia Alexandrov and Dr. Robert Biedron of NASA Langley Research Center and Dr. Boris Diskin of the National Institute of Aerospace for helpful discussions related to the current work.

References

[1] Biedron, R.T., and Lee-Rausch, E.M., "Rotor Airloads Prediction Using Unstructured Meshes and Loose CFD/CSD Coupling," AIAA 2008-7341, August 2008.

[2] Boelens, O.J., van der Ven, H., Kok, J.C., and Prananta, B.B., "Rotorcraft Simulations Using a Sliding-Grid Approach," 34th European Rotorcraft Forum, Liverpool, UK, Sept. 16-19, 2008.

[3] Lee, H.-K., Yoon, S.-H., Shin, S.J., and Kim, C., "Coupled CFD/CSD Analysis of a Hovering Rotor Using High Fidelity Unsteady Aerodynamics and a Geometrically Exact Rotor Blade Analysis," Presented at the 34th European Rotorcraft Forum, Liverpool, UK, Sept. 16-19, 2008.

[4] Lorber, P.F., Bagai, A., and Wake, B.E., "Design and Evaluation of Slatted Airfoils for Improved Rotor Performance," American Helicopter Society, 62nd Annual Forum, Phoenix, AZ, May 9-11, 2006.

[5] Narramore, J.C., Lancaster, G., and Sheng, C., "Application of Computational Fluid Dynamics During the Conceptual Design of the Bell JHL Quad Tiltrotor," American Helicopter Society, 63rd Annual Forum, Virginia Beach, VA, May 1-3, 2007.

[6] O'Brien, D.M., Calvert, M.E., and Butler, S.L., "An Examination of Engine Effects on Helicopter Aeromechanics," Specialist's Conference on Aeromechanics, San Francisco, CA, Jan. 23-25, 2008.

[7] Potsdam, M., Yeo, Y., and Johnson, W., "Rotor Airloads Prediction Using Loose Aerodynamic/Structural Coupling," *Journal of Aircraft*, Vol. 43, No. 3, 2006, pp. 732-742.

[8] Steijl, R. and Barakos, G., "Computational Analysis of Rotor-Fuselage Interactional Aerodynamics Using Sliding-Plane CFD Method," 34th European Rotorcraft Forum, Liverpool, UK, Sept. 16-19, 2008.

[9] Tanabe, Y., and Saito, S., "An Integrated Analysis Code with CFD/Rotor Dynamics Coupling Developed in JAXA," American Helicopter Society, Specialist's Conference on Aeromechanics, San Francisco, CA, Jan. 23-25, 2008.

[10] Modisette, J. M., "An Output-Based Adaptive and Higher-Order Method for a Rotor in Hover," M.S. Thesis, Dept. of Aeronautics and Astronautics, Massachusetts Inst. Of Technology, January 2008.

[11] Nielsen, E.J., and Park, M.A., "Using An Adjoint Approach to Eliminate Mesh Sensitivities in Computational Design," *AIAA Journal*, Vol. 44, No. 5, pp. 948-953.

[12] Park, M.A., and Darmofal, D.L., "Output-Adaptive Tetrahedral Cut-Cell Validation for Sonic Boom Prediction," AIAA 2008-6594, August 2008.

[13] Venditti, D.A., "Grid Adaptation for Functional Outputs of Compressible Flow Simulations," Ph.D. Dissertation, Dept. of Aeronautics and Astronautics, Massachusetts Inst. Of Technology, 2002.

[14] Newman III, J.C., Taylor III, A.C., Barnwell, R.W., Newman, P.A., and Hou, G.J.-W., "Overview of Sensitivity Analysis and Shape Optimization for Complex Aerodynamic Configurations," *Journal of Aircraft*, Vol. 36, No. 1, 1999, pp. 87-96.

[15] Choi, S., Lee, K.H., Alonso, J.J., and Datta, A., "Preliminary Study on Time-Spectral and Adjoint-Based Design Optimization of Helicopter Rotors," American Helicopter Society, Specialist's Conference on Aeromechanics, San Francisco, CA, Jan. 23-25, 2008.

[16] Mavriplis, D.J., "Solution of the Unsteady Discrete Adjoint for Three-Dimensional Problems on Dynamically Deforming Unstructured Meshes," AIAA 2008-727, January 2008.

[17] Nielsen, E.J., Diskin, B., and Yamaleev, N.K., "Discrete Adjoint-Based Design Optimization of Unsteady Turbulent Flows on Dynamic Unstructured Grids," AIAA 2009-3802, June 2009.

[18] Anderson, W.K., and Bonhaus, D.L., "An Implicit Upwind Algorithm for Computing Turbulent Flows on Unstructured Grids," *Computers and Fluids*, Vol. 23, No. 1, 1994, pp. 1–21.

[19] Anderson, W.K., Rausch, R.D., and Bonhaus, D.L., "Implicit/Multigrid Algorithms for Incompressible Turbulent Flows on Unstructured Grids," *Journal of Computational Physics*, Vol. 128, 1996, pp. 391-408.

[20] Nielsen, E.J., "Aerodynamic Design Sensitivities on an Unstructured Mesh Using the Navier-Stokes Equations and a Discrete Adjoint Formulation," Ph.D. Dissertation, Dept. of Aerospace and Ocean Engineering, Virginia Polytechnic Inst. and State Univ., December 1998.

[21] Biedron, R.T., and Thomas, J.L., "Recent Enhancements to the FUN3D Flow Solver for Moving-Mesh Applications," AIAA 2009-1360, January 2009.

[22] Roe, P.L., "Approximate Riemann Solvers, Parameter Vectors, and Difference Schemes," *Journal of Computational Physics*, Vol. 43, No. 2, 1981, pp. 357–372.

[23] Spalart, P.R. and Allmaras, S.R., "A One-Equation Turbulence Model for Aerodynamic Flows," AIAA 92-0439, 1991.

[24] Dacles-Mariani, J., Zilliac, G. G., Chow, J. S. and Bradshaw, P., "Numerical/Experimental Study of a Wingtip Vortex in the Near Field," *AIAA Journal*, Vol. 33, No. 9, 1995, pp. 1561-1568.

[25] Saad, Y., and Schultz, M.H., "GMRES: A Generalized Minimal Residual Algorithm for Solving Nonsymmetric Linear Systems," *SIAM Journal of Scientific and Statistical Computing*, Vol. 7, No. 3, 1986, pp. 856-869.

[26] Nielsen, E.J. and Anderson, W.K., "Recent Improvements in Aerodynamic Design Optimization on Unstructured Meshes," *AIAA Journal*, Vol. 40, No. 6, 2002, pp. 1155–1163.

[27] Nielsen, E.J., Lu, J., Park, M.A., and Darmofal, D.L., "An Implicit, Exact Dual Adjoint Solution Method for Turbulent Flows on Unstructured Grids," *Computers and Fluids*, Vol. 33, No. 9, 2004, pp. 1131-1155.

[28] Samareh, J.A., "A Novel Shape Parameterization Approach," NASA TM-1999-209116, May 1999.

[29] Kreisselmeier, G., and Steinhauser, R., "Systematic Control Design by Optimizing a Vector Performance Index," International Federation of Active Controls Symposium on Computer-Aided Design of Control Systems, Zurich, Switzerland, August 29-31, 1979.

[30] Wrenn, G.A., "An Indirect Method for Numerical Optimization Using the Kreisselmeier-Steinhauser Function," NASA CR 4220, March 1989.

[31] Kaufman, L. and Gay, D., "PORT Library: Optimization and Mathematical Programming - User's Manual," Bell Laboratories, 1997.

[32] Gill, P.E., Murray, W., Saunders, M.A., and Wright, M.H., "User's Guide for NPSOL 5.0: A FORTRAN Package for Nonlinear Programming," Technical Report SOL 94, 1995.

[33] Young, L.A., Booth Jr., E. R., Yamauchi, G.K., Botha, G., and Dawson, S., "Overview of the Testing of a Small-Scale Proprotor," American Helicopter Society 55th Annual Forum, Montreal, Canada, May 1999.

[34] Swanson, S. M., McCluer, M. S., Yamauchi, G.K., and Swanson, A. A., "Airloads Measurements from a 1/4-Scale Tiltrotor Wind Tunnel Test," 25th European Rotorcraft Forum, Rome, Italy, September 1999.

[35] Pirzadeh, S., "Three-Dimensional Unstructured Viscous Grids by the Advancing Front Method," *AIAA Journal*, Vol. 34, No. 1, Jan. 1996, pp. 43–49.

[36] Lyness, J.N., "Numerical Algorithms Based on the Theory of Complex Variables," Proc. ACM 22nd Nat. Conf., Thomas Book Co., Washington, DC, 1967, pp. 124-134.

[37] Lyness, J.N., and Moler, C.B., "Numerical Differentiation of Analytic Functions," *SIAM Journal of Numerical Analysis*, Vol. 4, 1967, pp. 202-210.

[38] Anderson, W.K., Newman, J.C., Whitfield, D.L., and Nielsen, E.J., "Sensitivity Analysis for the Navier-Stokes Equations on Unstructured Meshes Using Complex Variables," *AIAA Journal*, Vol. 39, No. 1, 2001, pp. 56-63.

[39] Kleb, W.L., Nielsen, E.J., Gnoffo, P.A., Park, M.A., and Wood, W.A., "Collaborative Software Development in Support of Fast Adaptive AeroSpace Tools (FAAST)," AIAA 2003-3978, 2003.

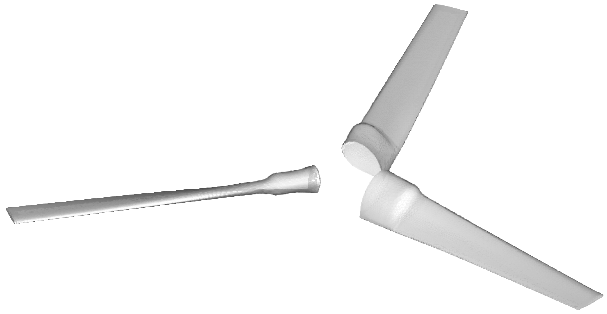

Figure 1. Surface geometry for TRAM rotor.

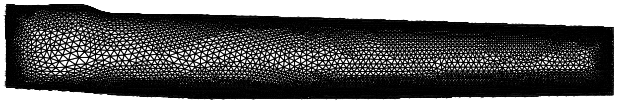

Figure 2. Typical blade surface grid used for design computations.

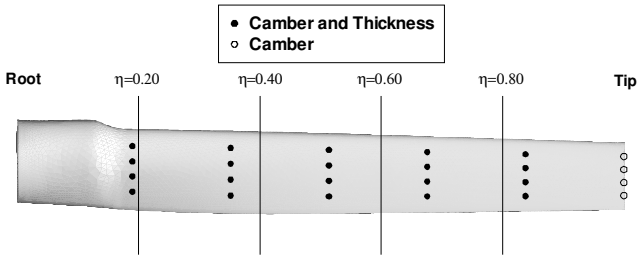

Figure 3. Design variable and radial blade locations.

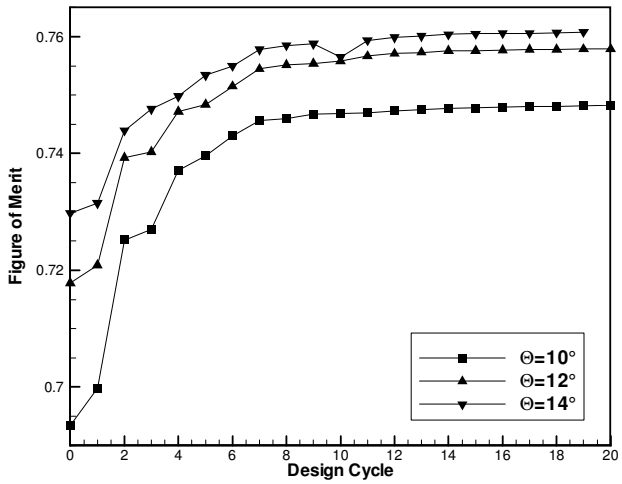

Figure 4. Figure of merit histories for optimizations with no thickness constraints included.

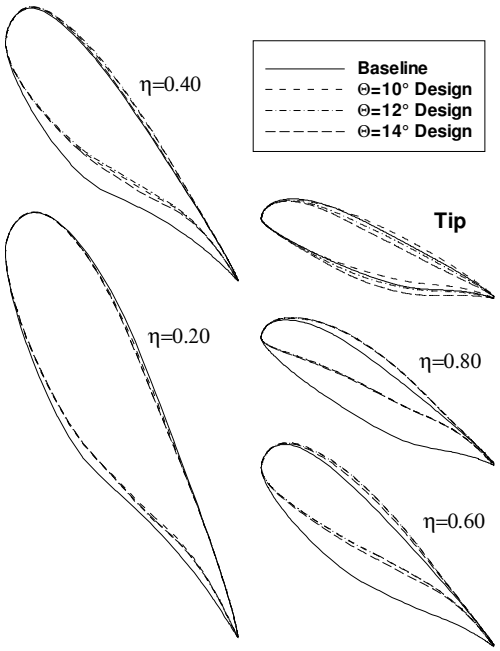

Figure 5. Blade cross-sections at various radial stations before and after optimization with no thickness constraints included. The vertical scale has been exaggerated and all blades have been rotated to the $\Theta = 14^{\circ}$ collective setting for comparison.

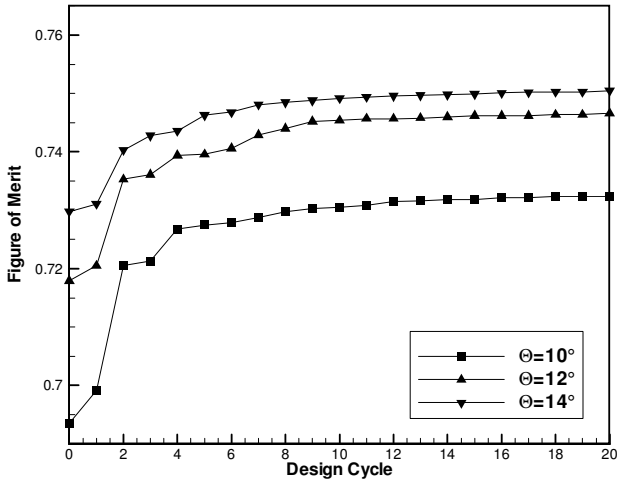

Figure 6. Figure of merit histories for optimizations with thickness constraints included.

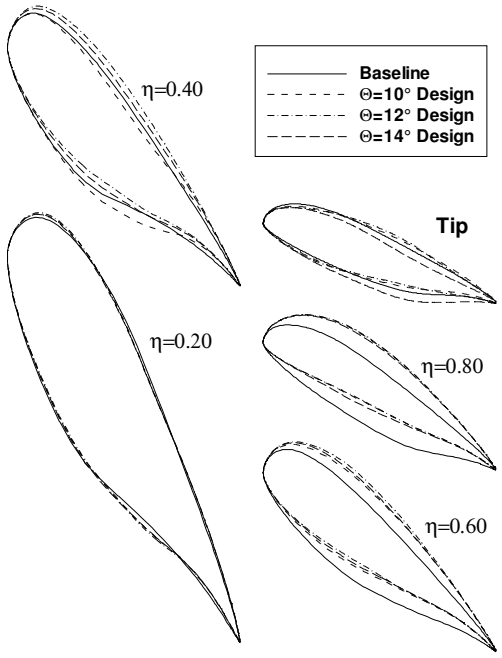

Figure 7. Blade cross-sections at various radial stations before and after optimization with thickness constraints included. The vertical scale has been exaggerated and all blades have been rotated to the $\Theta = 14^{\circ}$ collective setting for comparison.

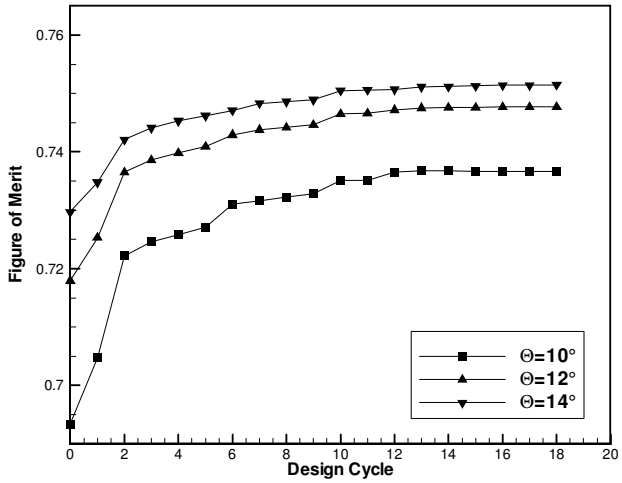

Figure 8. Figure of merit histories for multi-point optimization based on linear combination of objective functions given by Eq. (17).

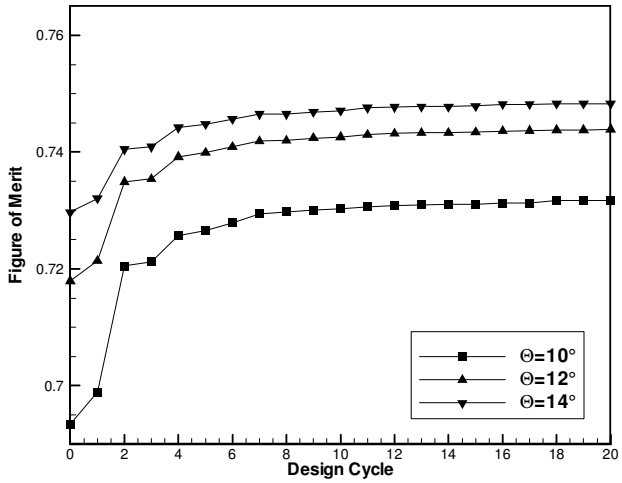

Figure 9. Figure of merit histories for multi-point optimization based on KS function given by Eq. (18).

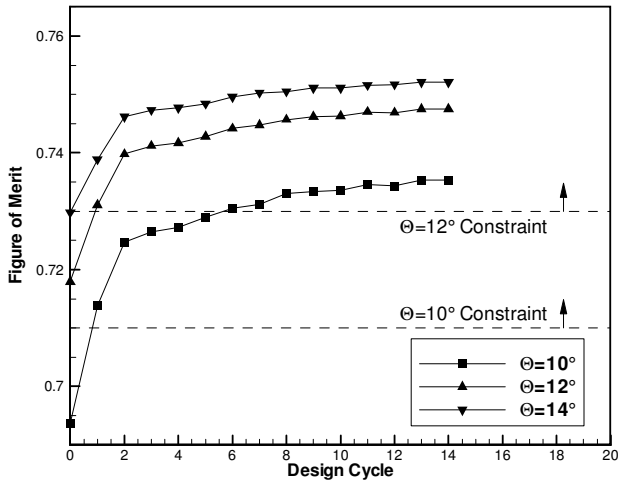

Figure 10. Figure of merit histories for multi-point optimization based on explicitly constrained approach (arrows indicate feasible side of constraints).

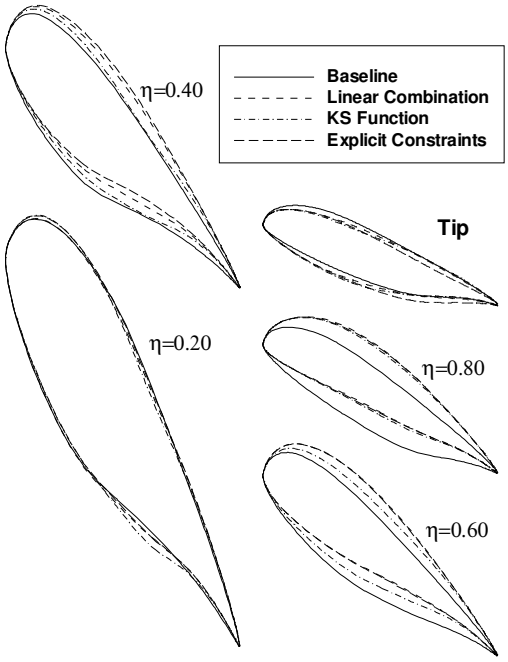

Figure 11. Blade cross-sections at various radial stations before and after multi-point optimization using the three different strategies considered. The vertical scale has been exaggerated and all blades have been rotated to the $\Theta = 14^{\circ}$ collective setting for comparison.

Table 1. Comparison of figure of merit sensitivity derivatives obtained by using adjoint and complex variable approaches. "A" denotes adjoint result, "C" denotes complex-variable result.

Design Variable	$\partial(FM)/\partial\mathbf{D}$
Twist	A: 0.000396489658597 C: 0.000396489658593
Thickness	A: 0.002169495035056 C: 0.002169495035076
Camber	A: 0.004203140874745 C: 0.004203140874793

Table 2. Figure of merit before and after single point designs with no thickness constraints.

Θ	Initial *FM*	Final *FM*	ΔFM	Percent Change
10°	0.693	0.748	0.055	7.9%
12°	0.718	0.758	0.040	5.6%
14°	0.730	0.761	0.031	4.3%

Table 3. Figure of merit before and after single point designs with thickness constraints included.

Θ	Initial *FM*	Final *FM*	ΔFM	Percent Change
10°	0.693	0.732	0.039	5.6%
12°	0.718	0.747	0.029	4.0%
14°	0.730	0.751	0.021	2.9%

Table 4. Figure of merit before and after multi-point optimization based on linear combination of objective functions given by Eq. (17). Values in parentheses represent results on refined grid.

Θ	Initial *FM*	Final *FM*	ΔFM	Percent Change
10°	0.693 (0.734)	0.737 (0.776)	0.044 (0.042)	6.3% (5.7%)
12°	0.718 (0.758)	0.748 (0.785)	0.030 (0.027)	4.2% (3.6%)
14°	0.730 (0.768)	0.752 (0.787)	0.022 (0.019)	3.0% (2.5%)

Table 5. Figure of merit before and after multi-point optimization based on KS function given by Eq. (18). Values in parentheses represent results on refined grid.

Θ	Initial *FM*	Final *FM*	Δ*FM*	Percent Change
10°	0.693 (0.734)	0.732 (0.772)	0.039 (0.038)	5.6% (5.2%)
12°	0.718 (0.758)	0.744 (0.783)	0.026 (0.025)	3.6% (3.3%)
14°	0.730 (0.768)	0.748 (0.785)	0.018 (0.017)	2.5% (2.2%)

`

Table 6. Figure of merit before and after multi-point optimization based on explicitly constrained approach. Values in parentheses represent results on refined grid.

Θ	Initial *FM*	Final *FM*	Δ*FM*	Percent Change
10°	0.693 (0.734)	0.735 (0.773)	0.042 (0.039)	6.1% (5.3%)
12°	0.718 (0.758)	0.748 (0.784)	0.030 (0.026)	4.2% (3.4%)
14°	0.730 (0.768)	0.752 (0.788)	0.022 (0.020)	3.0% (2.6%)